A Microtissue Platform to Simultaneously Actuate and Detect Mechanical Forces via Non-Contact Magnetic Approach

Josh Javor [ID], Subramanian Sundaram [ID], *Member, IEEE*, Christopher S. Chen, and David J. Bishop, *Member, IEEE*

Abstract—**Mechanical control is essential for adaptive regulation in biological systems. This work presents a magnetic, non-contact approach to simultaneous detection and actuation in a microscale tissue testbed. The platform builds upon previously developed passive mechanical platforms, where tissues self-assemble on flexible pillars. Standard detection is typically derived from microscope images and actuation is often conducted using invasive approaches. In the presented platform, actuation and detection, both derived from magnetic fields, are demonstrated with high spatial, temporal, and force resolution resulting in a detectable 0.6 μm step-size in air. The forced deflection range is $+/-125$ microns ($+/-10\%$ strain), and an arbitrary magnitude step-and-settle actuation is achieved in less than 1 ms. Engineered human cardiac microtissue is used to demonstrate the capabilities of the system, as cardiac tissues generate contractions and adapt to external forces. Spontaneous contractions are monitored for an hour by a built-in sensor with a signal-to-noise of 2. Cyclic actuation at 1 Hz using a 1 mT/mm magnetic field is demonstrated, where max tissue strain is 0.3%. All this is achieved in a moderate-throughput, compact device, which is easily integrated into the typical flow of biological experimentation. Simultaneous control of actuation and detection enables decisions to be made on a sample-specific basis, and in future developments, will enable arbitrary design of the mechanical environment for 3D tissue conditioning, maturation, and control.** [2020-0296]

Index Terms—**BioMEMS, microtissue, tissue mechanics, organ-on-a-chip, cardiac tissue engineering, hiPSC-CMs, maturation.**

I. Introduction

MECHANICAL forces play a significant role in the function and maturation of all biological tissues [1]–[3]. Multiscale platforms have been instrumental in the study of

Josh Javor is with the Department of Mechanical Engineering, Boston University, Boston, MA 02215 USA (e-mail: jjavor@bu.edu).

Subramanian Sundaram and Christopher S. Chen are with the Department of Biomedical Engineering, Boston University, Boston, MA 02215 USA (e-mail: subramanian.s88@gmail.com; chencs@bu.edu).

David J. Bishop is with the Division of Material Science and Engineering, Department of Electrical and Computer Engineering, Boston University, Boston, MA 02215 USA, also with the Department of Physics, Boston University, Boston, MA 02215 USA, also with the Department of Mechanical Engineering, Boston University, Boston, MA 02215 USA, and also with the Department of Biomedical Engineering, Boston University, Boston, MA 02215 USA (e-mail: djb1@bu.edu).

cell and tissue scale forces [1]–[18]. While 2D and cellular scale systems have developed significantly [4], [5], 3D and tissue scale platforms are more relevant to the native environment [3], [6]–[11]. Many 3D tissue platforms have converged on a similar micromechanical design, where the forces are simplified to a single axis and the tissue is small such that nutrients permeate the tissue without a need for complex vasculature [1], [6]–[9].

From a mechanical perspective, there are levels of complexity in the load profile that can be imposed on a 3D tissue. A rigid platform is isometric, meaning the length of the sample does not change. A passive platform may deflect in response to tissue forces, but the platform mechanics are constant during the experiment, and the load profile is often linearized for simplicity. An active platform incorporates changing mechanics, such as forced contraction of a tissue or stiffening the environment slowly over time. An active platform with simultaneous, real-time detection would inspire unprecedented, sample-specific actuation experiments, such as triggered contraction or controlled baseline tension.

Mechanical force control is ubiquitous in the biological world, where self-sustaining mechanisms regulate homeostasis and mechanical forces. Although common to all biological tissues, cardiac tissue serves as an ideal example of mechanical control. In the native heart, pacemaker cells coordinate the contraction of billions of cells, timed perfectly to oxygenate blood and pump it throughout the body. The most physiologically relevant engineered heart tissue (from human induced pluripotent stem cell-derived cardiomyocytes, or hiPSC-CMs) also exhibits coordinated contraction, albeit slower and with less force. These hallmarks of immaturity have been greatly improved by the aforementioned 3D tissue platforms, where advanced design of the mechanical environment plays a critical role [8], [10], [12]. Active platforms have demonstrated the ability to trigger contraction [13], improve maturation [10], [14]–[16], and characterize drug response [11], [17]. To more fully characterize how biological tissues respond to their mechanical environment, new tools are necessary to facilitate active force control while simultaneously measuring tissue contractile activity.

In this work, we expand on a recently published conference paper [1] to present a platform with active mechanical control and simultaneous detection, both via magnetic approaches (Fig. 1). Our method enables bidirectional, arbitrary waveform force profiles, actuation and detection are conducted without contact, and long-term monitoring in a controlled environment.
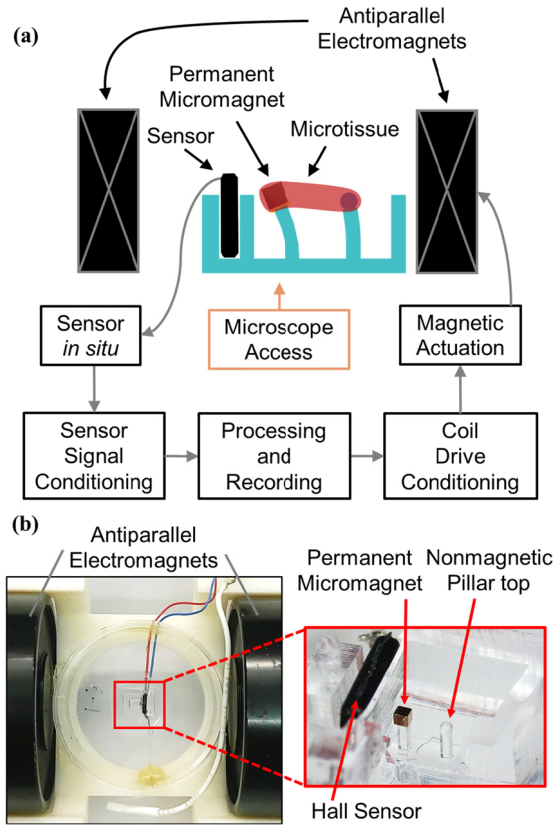
Fig. 1. Tissue platform with simultaneous actuation and detection., where both mechanisms are magnetic and non-contact. (a) Actuation is conducted via a magnetic force (gradient magnetic field) on an embedded permanent micromagnet, and is compatible with bipolar, arbitrary waveforms. The position of the micromagnet is detected by a Hall sensor (uniform magnetic field). Simultaneous optical access from a microscope is also shown. The system is constructed for experimentation using mechanical feedback control. (b) Photograph of assembled system and cross-section of device (inset).
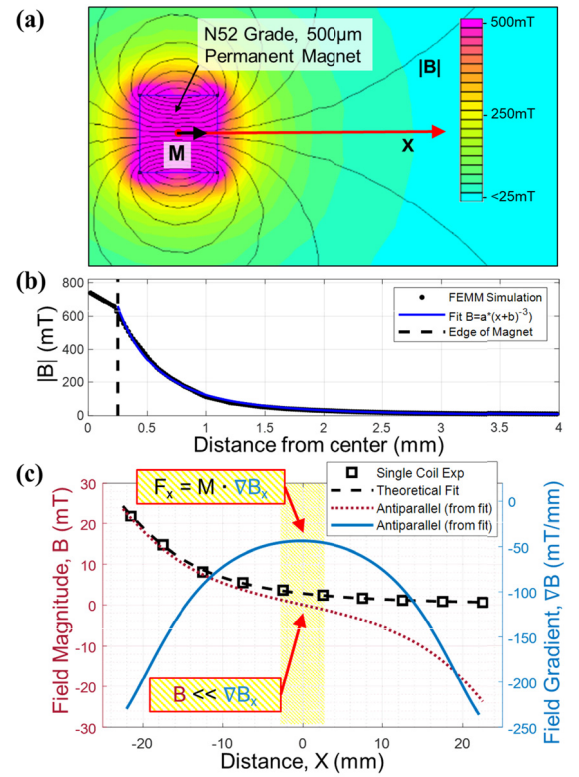

Fig. 2. Design of actuation. (a) Magnetic field simulation of micromagnet for moment calculation; (b) Fit along magnet axis in (a); (c) characterization of anti-parallel electromagnetic coil pair for force generation via a gradient field.

The platform leverages the toolkit of microelectromechanical systems (MEMS), and focuses on throughput, compactness, and self-sufficiency. Finally, we use hiPSC-CMs in a 3D microtissue to demonstrate the biocompatibility and a high-impact application of the platform.

II. METHODS

A. Design of Micromagnet

The dipole moment of the micromagnet is determined from a simulation along its central axis (Fig. 2a). A 500 μm long, N52 grade magnet is drawn in magnetic simulation software (FEMM), and the uniform field profile is gathered along its central axis (Fig. 2b). The simulation agreed well with experimental measurements, where the magnetic field at the face of the magnet was measured to be approximately 600 mT, as measured by a Hall sensor (A1359). The profile can then be fit by Eq. 1 [18], where: magnetic field is $\vec{B}_{mag}$, M_0 is the magnetic permeability of air, $\vec{M}_{mag}$ is the moment of the micromagnet, and $\vec{r}_{mag}$ is the distance from the center of the magnet along the dipole axis. Knowing the other quantities, the magnetic moment can be extracted from the fit

as 15 μJ/T.

$$\vec{B}_{mag} = \frac{2M_0 \vec{M}_{mag}}{4\pi} \left(\frac{1}{\vec{r}_{mag}}\right)^3 \quad (1)$$

B. Design of Magnetic Actuation

The coils are wired in an antiparallel configuration, giving rise to a gradient magnetic field and minimizing the field magnitude at the centered location of the micromagnet. A distance profile of both magnitude and gradient field along the central axis of the coil pair (one axis of the dish and common to dipole axis of micromagnet) is shown for a current 50 times larger than a typical experiment (Fig. 2c). First, a single coil is characterized along its central axis (black squares) at 300mA. This profile is fit (black, dashed line) using the relationship given by Eq. 2, where: $\vec{B}_{coil1}$ is the uniform magnetic field along the central X-axis, N is number of turns, k is the relative permeability of the core, M_0 is the magnetic permeability of air, R is the radius of the coil, I is the current, and $\vec{X}$ is the distance from the center of the coil, along its central axis (see Fig. 1).

$$\vec{B}_{coil1} = N \frac{kM_0}{4\pi} \frac{\left(2\pi R^2\right) I}{\left(\vec{X}^2 + R^2\right)^{3/2}} \quad (2)$$

Since the two coils are identical, but the second coil is reversed in direction and spaced by a separation, d, from
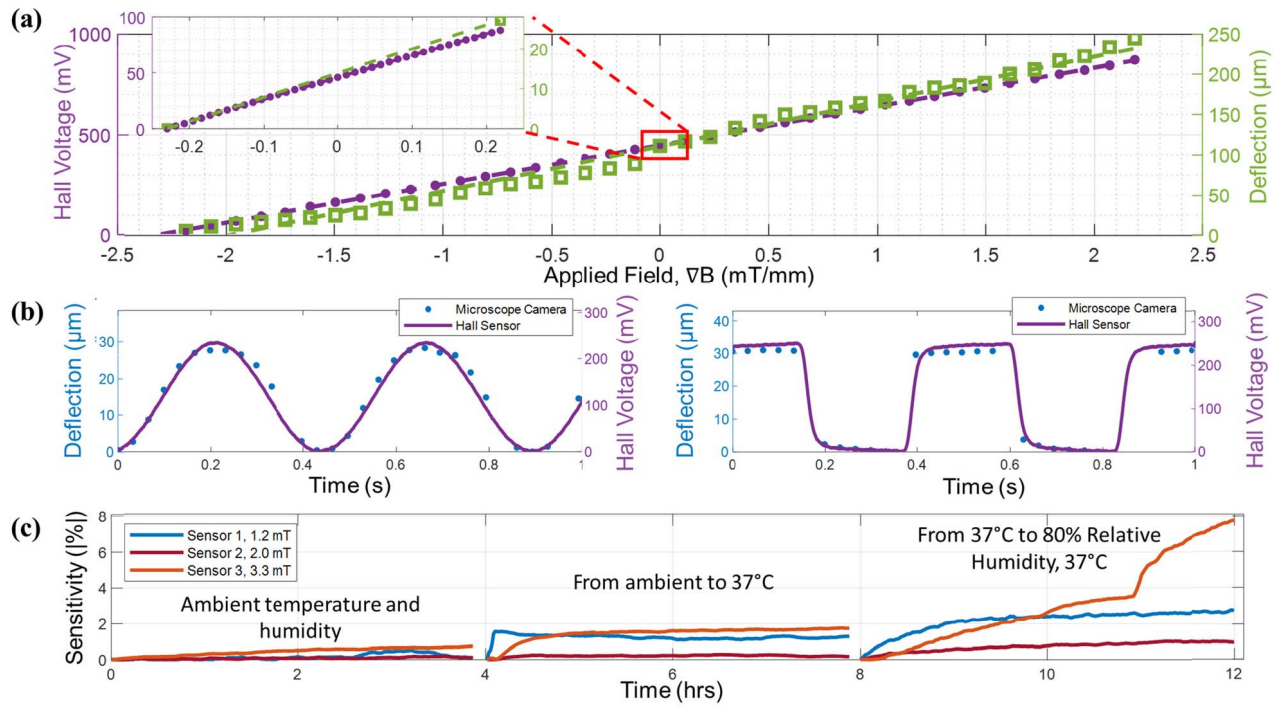
Fig. 3. Design of sensing. (a) Simultaneous, static position sensing using built-in Hall sensor and benchtop microscope images, demonstrating high actuation resolution, high sensing resolution, and large range; (b) simultaneous dynamic position sensing of sine (left) and square wave (right) using Hall sensor and microscope images; (c) sensitivity characterization of Hall sensor in ambient, elevated temperature, and elevated humidity conditions inside a biological incubator.

the first coil, the second coil's magnetic field, $\vec{B}_{coil2}$, can be calculated from Eq. 2 by plugging in new X-coordinates, shown in Eq. 3. The second coil is also opposite in sign from the first because the coils are in the anti-parallel configuration.

$$\vec{B}_{coil2} = -f\left(\vec{B}_{coil1}\right) = -\vec{B}_{coil1}(-\vec{X} + d) \quad (3)$$

The field magnitude, $\vec{B}_{ext,X}$, can be calculated by Eq. 4 and the field gradient, $\nabla\vec{B}_{ext,X}$, can be calculated by its spatial derivative along the central, X-axis in Eq. 5. Both Eq. 4 and 5 are plotted (Fig. 2c, red and blue respectfully), calculated from the single coil experimental data.

$$\vec{B}_{ext,X} = \vec{B}_{coil1} + \vec{B}_{coil2} \quad (4)$$

$$\nabla\vec{B}_{ext,X} = \frac{d\vec{B}}{d\vec{X}} \quad (5)$$

The antiparallel system is specifically designed so that the micromagnet will feel a uniaxial force without torque, and the Hall sensor will detect the micromagnet position, having minimal interference from a very low uniform field. A uniform magnetic field, $\vec{B}_{ext}$, would apply an unwanted torque, $\vec{T}$, to a micromagnet of moment $\vec{M}_{mag}$ by Eq. 6 [18], and so is minimized by design. Coil design is important for minimizing torque (see *SI Appendix*, Fig. S2). A gradient magnetic field imposes a force, $\vec{F}$, on a micromagnet of moment $\vec{M}_{mag}$ by Eq. 7 [18]. The moment of the micromagnet was calculated

earlier in Eq. 1.

$$\vec{T} = \vec{M}_{mag} \times \vec{B}_{ext} \quad (6)$$

$$\vec{F} = \vec{M}_{mag} \cdot \nabla\vec{B}_{ext} \quad (7)$$

C. Design of Magnetic Detection

A Hall sensor (A1359) is chosen to detect the position of the micromagnet based on its size, speed, resolution, and bandwidth [19]. The sensor is aligned with the dipole axis of the micromagnet. The voltage reported by the sensor, $V_{Hall}(t)$, is proportional to $\vec{B}_{mag}$ in Eq. 1. The micromagnet is spaced a distance away from the Hall sensor such that it can still be detected (Fig. 1), and small deflections can be approximated by a linear change in magnetic field (or Hall voltage) in Eq. 8. A constant, γ, expresses the sensitivity and $d_{mag}(t)$ is the distance away from the sensor at a given point in time.

$$V_{Hall}(t) = \gamma * d_{mag}(t) \quad (8)$$

D. Calibration Using Benchtop Microscope

The experimental setup without biological tissue is characterized statically (Fig. 3a) and dynamically (Fig. 3b) by a benchtop microscope (Koolertron). Microscope settings are maximized magnification with 12M resolution for static images and 1080p resolution, 30 fps for videos. Magnet position is extracted from microscope images and videos (TrackMate, ImageJ). Characterization is conducted on the fully constructed experimental setup to maximize accuracy

of calibration. Using the electromagnetic actuation technique described earlier and a micromagnet fixed and oriented on a PDMS post, the gradient magnetic field is swept linearly from −2.4 to 2.4 mT/mm. The resulting range of deflection is approximately 250 μm on the microscope and 825 mV on the Hall sensor (Fig. 3a). A linear least square fit is used to calculate a slope for both sets of deflection data. The sensitivity, γ, from Eq. 8 can then be calculated by a ratio of these two slopes, resulting in 3.4 mV/μm. A fine sweep is conducted in the central region (Fig. 3a inset), confirming a linear relationship with a smallest step size of 11 μT/mm resulting in 2.25 mV and 0.6 μm deflection.

The setup is dynamically calibrated by cycling the micromagnet at 2.2 Hz and simultaneously recording a video and voltage trace (Fig. 3b). When extracting the magnet position from image frames, the particle tracker omits a data point if the feature is below a detection threshold, such as in a blurred image while the magnet is moving. A sine wave (left), square wave (right), and sawtooth (see *SI Appendix*, Fig. S3c) profile are demonstrated. The sine wave magnetic signal from the hall sensor has low distortion, indicating validity of the linear deflection approximation. The rise time and decay time on the square wave are not limited by the hall sensor (decay time of 750 μs [19]) but are instead limited by overdamped actuation from the electromagnetic coils. Open-loop drive techniques have been developed based on previous work [20], [21] to improve settling by over an order of magnitude and are demonstrated later (Fig. 6b and c).

Hall sensors are known to be affected by temperature and humidity, causing expansion of both the sensor package and Hall element [22]. Three sensors are inserted in separate devices with micromagnets (see *SI Appendix*, Fig. S3b) to characterize the response of the chosen sensor in incubator conditions. The micromagnets impose a static magnetic field between 1 and 3 mT on the hall sensor. Assuming this field stays constant throughout the experiment, the percent sensitivity change can be calculated from the recorded sensor voltage. A miniature incubator (MyTemp Mini) is used to impose stepwise conditions of elevated temperature and, subsequently, elevated humidity, each for 4 hours (Fig. 3c). The sensors stay within 1% in ambient conditions and within 2% in elevated temperature, where they exhibit a slow settling response. In elevated humidity, sensors again have a slow settling response. The relative expansion of several different materials may have caused sensor 2 to slip relative to the micromagnet, where a second step change is observed. The earliest recordings are typically taken after 5 days of tissue culture, at which point the sensor signals have stabilized.

E. CMT Deflection Tracking With Incubator Microscope

An inverted brightfield microscope (Nikon Eclipse Ti), is used to track deflection of pillars when a microtissue is present. Settings are 5X magnification and 30 fps. A custom MATLAB script is used to track the deflection of the pillars in sequential image frames by tracking features with steep image gradients. When a tissue is cultured on the device (Fig. 1h), the magnet edges are obscured upon tissue compaction, and
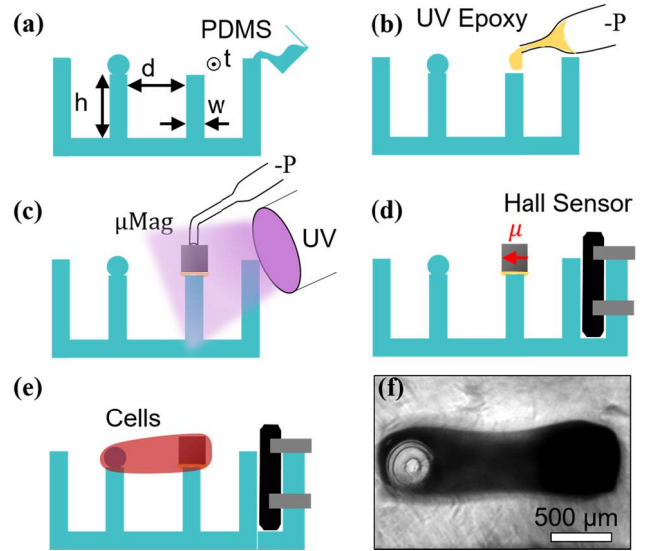

Fig. 4. Fabrication overview. (a) Polydimethylsiloxane (PDMS) microstructure; (b) application of UV epoxy; (c) functionalization with permanent micromagnet; (d) insertion of Hall sensor; (e) illustration and (f) microscope image of self-assembled microtissue on magnetically functionalized device.

therefore the deflection of a feature on the spherical pillar top is tracked. During actuation experiments with CMTs, the deflection of the nonmagnetic pillar and the applied force on the magnetic pillar are used to calculate tissue strain (assuming linear elastic properties of the microtissue). This technique is useful for quick measurements (under a minute), but large microscope image files may become burdensome for long-term monitoring.

III. FABRICATION

A. Elastomeric Microstructure

In essence, the device (Fig. 1b, right) consists of a magnetically functionalized tissue strain gauge (TUG) inspired by previous designs [6], [14], [17]. A mold is designed in-house (SolidWorks) and 3D-printed with dial-in tolerance (Protolabs). The mold is silanized overnight (Trichlorosilane, Sigma Aldrich) in vacuum to increase mold hydrophobicity and prevent sticking during removal. The platform material is polydimethylsiloxane (PDMS, Sylgard 184, Ellsworth), mixed in a 1:20 ratio of crosslinker to base. PDMS is mixed and poured into the mold before being degassed for 2 hrs. The mold cures overnight at 60°C and is carefully removed to keep micropillars intact. The cured structure (Fig. 4a) consists of a small, rectangular well (5.5 μL). Extruded from the base of the small well are two 800 μm tall pillars (h), separated 1.2 mm center-to-center (d), with 390 μm (w) by 430 μm (t) rectangular cross sections. The primary direction of deflection occurs along the thinner side-length (w). On the top of one pillar is a PDMS sphere of diameter 490 μm, which facilitates tissue attachment.

B. Magnet Passivation and Biocompatibility

The micromagnet is a neodymium-iron-boron cube with 500 μm side length, N52 magnetization strength, and a

typical outer coating of layered nickel, copper, and nickel (SM Magnetics). Several materials inside a permanent magnet and involved in industrial magnet manufacturing processes are cytotoxic in high concentrations, so each micromagnet is passivated by a custom coating to minimize leaching into the aqueous environment. An effective passivation coating for this platform needs to be biocompatible, conformal, resistant to degradation, thin (<15 μm), and capable of moderate throughput. The actuation and detection results reported here (Fig. 6) used a low-temperature atomic layer deposition (ALD) sapphire coating (Fig. 5) [23], and electroplated gold was found to be an optimum passivation coating for future work (Fig. S5).

C. Magnetic Functionalization and Tissue Culture

The flat-top pillar is functionalized with the passivated micromagnet using a custom vacuum pick-and-place system, as illustrated (Fig. 4 b-d). This system was previously developed for higher resolution fabrication on post-release silicon micro devices [21], [24], [25]. Probe station micropositioners (Cascade Microtech), coupled with glass micropipettes, are used for microscale fabrication. A straight pipette with 30 μm aperture (WVI) is used to apply epoxy to the flat-top pillar and a 45° bent pipette with 135 μm aperture (Clunbury Scientific) is used to align and assemble magnets. Light vacuum (<1 psi) is applied on the straight pipette near UV-curable epoxy (NOA81, Norland Adhesives) to load the pipette. The pipette is brought into contact with the top of the flat pillar and vacuum is controllably decreased to deposit a few microliters on top of the pillar. Next, the micromagnet is held on a stationary vertical glass slide and oriented horizontally by an external magnet. The tip of the bent pipette is brought into contact with the top of the micromagnet, and vacuum (>2 psi) is applied. The pipette and micromagnet are then moved together under a microscope and positioned over the flat-top pillar (Fig. 4c), where the epoxy is spot-cured by focused UV light (Bluewave, Dymax). The procedure takes approximately 15 min per device, and typical alignment on 8 devices is characterized by optical profilometer images (Fig. S1). Assembled devices are screened if micromagnets have a tilt magnitude greater than 5 degrees or if they produce a field less than 1 mT at the face of the Hall sensor.

The magnetically functionalized PDMS structure is centered in a standard 35 mm petri dish (Falcon) and PDMS is poured around the structure and cured. For detection experiments, a Hall sensor (A1359, Allegro MicroSystems) is easily inserted into a predesigned pocket in the PDMS mold (Fig. 4d). Leads carrying power and output signal are soldered and passivated using PDMS. The leads extend from the sensor and out of the petri dish through small holes that are resealed with epoxy.

At this point, the microtissue is seeded and allowed to compact around the pillar tops (Fig. 4e and f). For hiPSC-derived cardiac microtissues used in this work, a previous procedure is expanded on for larger, millimeter-long tissues [6]. The microtissue, comprising approximately 60,000 cells (9:1 iPSC-CM: human mesenchymal stem cells), is cultured such that cells are uniformly distributed in a Fibrin gel, and self-assemble around the pillars, compacting to form a condensed
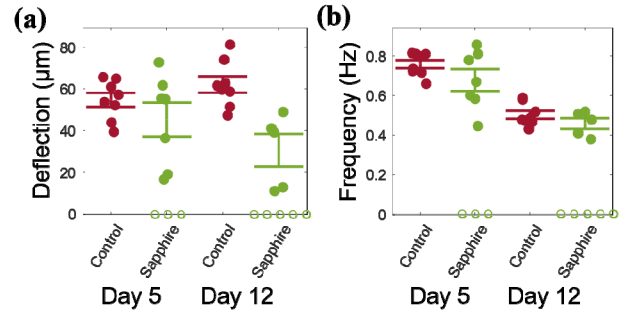

Fig. 5. Biocompatibility characterization of magnetically functionalized devices where permanent magnet is passivated with sapphire. Spontaneous contractions are tracked by a microscope, extracting deflection (a) and frequency (b) on day 5 and 12 after seeding. Each data point represents multiple contractions from a different device and tissue sample. There are 8 controls and 10 tests (3 of latter without contractions). Further characterization with parylene and gold is shown in Fig. S5.

microtissue [26] over the course of 2 to 4 days. A complete device is illustrated from a side-view (Fig. 4e) and pictured from a top-view (Fig. 4f). The tissue self-assembles at the tops of the pillars, around both the PDMS sphere (left) and micromagnet (right).

D. Device Holder

The petri dish is press-fit into a 3D-printed holder, orienting and centering it between two concentric electromagnets (P50/27, Uxcell). The holder is designed, so to allow simultaneous optical access by a brightfield microscope (Fig. 1b, h). To monitor multiple devices for long periods of time, the holders are placed in an incubator (37°C, 5% CO_2). The wires are carried through a port to processing and recording equipment outside.

IV. RESULTS AND DISCUSSION

A. Platform Biocompatibility

To evaluate biocompatibility of the passivation coating, spontaneous contractions of hiPSC-CMTs are tracked on the platform at day 5 and day 12 after seeding (Fig. 5). Each data point represents multiple contractions and a unique device and tissue. The controls are devices without a magnet. Both contractile deflection and frequency, are compared. Tissues that did not contract within several minutes of observation are recorded as an open-circle data point at the bottom of the plot. For frequency recording, tissues that did not contract more than once during a 15-second time frame are also included in the open-circle points. Compared to controls, several tissues grown on devices with magnets appear to have lower, more variable deflections and frequencies, and some show no deflections at all. This may be due to unintended toxin exposure during the custom passivation stage or the magnet handling stages of fabrication (conducted in an electronics lab). It was qualitatively observed that hiPSC-CMTs are very sensitive to the introduction of many materials and so the cleanliness of the fabrication procedure was improved for future experiments (Fig. S5). To address this, alternative passivation techniques were developed and extensively characterized (Fig. S5). A gold electroplating technique was found to be the most favorable

with all tissues showing contractions at day 12, and average deflections and frequencies in the range of the control (Fig. S5a).

B. CMT Actuation

Cyclic magnetic actuation of a spontaneously contracting hiPSC-CMT is demonstrated over 15s, recorded by the microscope (Fig. 6a and b). A representative CMT contracts spontaneously without actuation (Fig. 6a, video S3). After 5 days of culture, the contraction amplitude is 1-2 μm deflection, which is at the low end of the range of previously reported hiPSC-CMTs [8], [10]. The tissue deflects both pillars symmetrically with a typical profile comprising a steep increase (upstroke) followed by a slower relaxation. The external force felt by the tissue increases linearly with deflection (for small deflections) [6]. Even in the short, 15s window showing 6 contractions, variation in frequency and contraction profile can be observed. These characteristics may be manipulated and improved by electrical or mechanical training [8], [10], [13].

The same tissue is used minutes later to demonstrate actuation (Fig. 6b, video S4). The magnetic pillar is actuated by a 1 Hz, 1 mT/mm peak-to-peak sinusoidal gradient magnetic field, resulting in a bidirectional, cyclic strain of 0.3%. Throughout actuation, the tissue beating can still be observed by constructive and destructive deflections, labeled on the plot. This is because the frequency and phase of the actuation is not synchronized with CMT contractions, which would require feedback control. Mechanical training at a fixed frequency at or faster than spontaneous contractions may stabilize the contraction frequency or increase it on average [10], [13].

Although mechanical actuation of 3D microtissues has been implemented by commercially available tissue stretchers [10], [11] and control of embedded magnets [14], [17], platforms have not been designed for feedback control. Low frequency actuation at or slightly higher than the spontaneous contraction frequency of a tissue may be useful for mechanical training [10], [13]. High frequency actuation may be useful for the study of some pathologies, such as tachycardia, as has been shown previously on a well-developed, 2D microelectrode array (MEA) platform [5]. A high range of actuation, such as 30% strain, is useful in characterizing features such as the Frank-Starling relationship in hiPSC-CMTs [9]–[11]. The presented platform is primarily designed for feedback actuation but may also be useful for actuation in early stages of maturation (as the tissue does not need to be transplanted onto a stretching platform), as well as for long-term, bidirectional actuation.

C. CMT Detection

Spontaneous deflections of a representative hiPSC-CMT are monitored for approximately an hour inside an incubator and post-processed (Fig. 6c and d). The measurements are recorded with no light and in an incubator. The CMT (different from Fig. 6a and b) is measured on day 10 after seeding. Hundreds of spontaneous contraction peaks are detected with a signal-to-noise ratio (SNR) of about 2. An abridged, 15s window of unprocessed data is shown (Fig. 6c) to facilitate comparison between real-time sensing and post-processed deflection
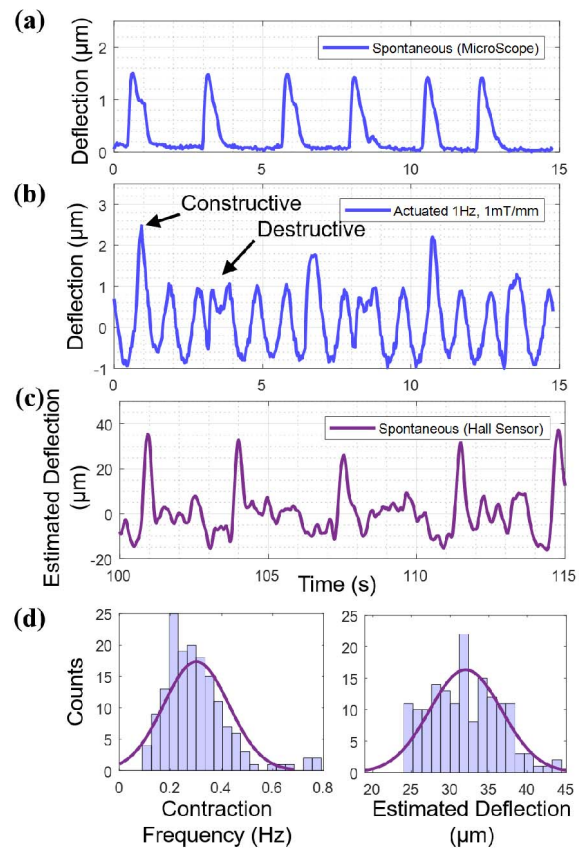

Fig. 6. Actuation and sensing of human induced pluripotent stem cell derived (hiPSC) cardiac tissue: (a) spontaneous contractions post-processed from microscope images, (b) bidirectional magnetic actuation including superposition of spontaneous contractions, extracted from microscope images, (c) raw data from non-contact sensor depicting spontaneous contractions during hour-long monitoring inside incubator, (d) frequency and deflection histograms from processed sensor recording. These data are from a single representative sample, where further detail is presented in Fig. S6.

images (Fig. 6a). The present SNR of the platform is likely limited by the Hall sensor in fluctuating temperature and humidity conditions, as shown earlier (Fig. 3c).

In addition to actuation, the signal can be recorded and post-processed later in MATLAB (Fig. S6). Despite the low SNR, the timing and amplitude of contractions are extracted. Timing will be more accurate than deflection amplitude, for the present design. However, accuracy of the deflection amplitude may be improved by averaging multiple, consecutive peaks (assuming the contraction profile is unchanging from one contraction to the next). Histograms of contraction amplitude and frequency are depicted for 10min of the recording (Fig. 6d), and for subsequent segments (Fig. S6b). Contractions are counted, binned, and fit by a normal distribution. The average frequency of contraction is 0.30 Hz with a standard deviation of 0.13 Hz. Similarly, the average deflection is 32 μm with a standard deviation of about 5 μm. This large variation in contraction frequency and amplitude suggest an opportunity for experiments to impose greater mechanical control.

While microscopes offer the standard detection of hiPSC-CMT contraction and this is useful for many aspects of biological research [6]–[10], [13]–[15], there are several limitations. The high resolution for deflection is achieved after

This article has been accepted for inclusion in a future issue of this journal. Content is final as presented, with the exception of pagination.

JAVOR *et al.*: MICROTISSUE PLATFORM TO SIMULTANEOUSLY ACTUATE AND DETECT MECHANICAL FORCES 7
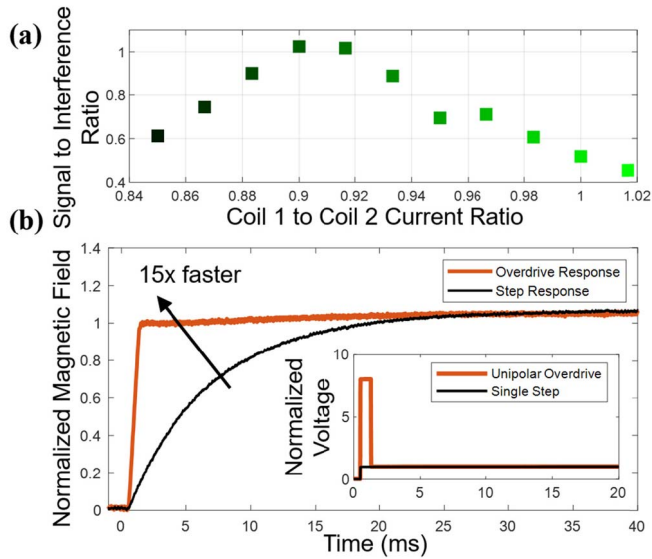

Fig. 7. Optimization for closed-loop control: (a) reducing magnetic interference from actuation, (b) utilizing an electromagnetic drive technique to increase speed of actuation.

image post-processing, a technique that may not be compatible with real-time feedback. The frame rate is limited by trade-offs in other settings such as the field of view and magnification. The total length of the recording is limited by computer storage of large image files and is also practically affected by the quality of temperature and humidity control in the microscope chamber. Only one tissue can be tracked at a time, which makes discerning the effects of temperature and humidity changes more difficult. In the presented platform, multiple tissues can more easily be tracked simultaneously and the availability of real-time data offers an opportunity for experiments with feedback control. Furthermore, we discovered that the platform may be useful for long-term contraction frequency monitoring in a highly controlled environment (Fig. S4 and S6).

D. Toward Closed-Loop Feedback Control

In order to close the loop, interference between electromagnetic actuation and Hall-effect magnetic detection must be minimized. Interference is characterized on a fully functionalized platform, without a microtissue, and an optimization procedure is developed and illustrated (Fig. S7). Various asymmetries (such as coil wire length, number of turns, coil pair alignment, sensor alignment, etc.) may contribute to interference. In order to analyze interference, the signal from the micromagnet motion and from the electromagnets must be decoupled. For large-deflection actuation, the signal from the micromagnet becomes cubic (where the small-deflection approximation breaks down). Since the magnetic fields add at the face of the Hall sensor, the cubic profile from the micromagnet and the sinusoidal profile from the coils can be isolated by independent fits (Fig. S7b). The interference signal is then minimized by tuning the current amplitude ratio between the magnetic coils to minimize interference (Fig. 7a). This is effectively a calibration, as the ratio is fixed and remains constant throughout an experiment. The

optimized signal to interference ratio is just above 1 for the present design. While this may limit more complex feedback experiments, this is sufficient for those that involve time-based triggering (further detail in Fig. S8).

Here, electromagnetic actuation requires driving moderate current amplitudes through large coils of wire, which can dampen a signal and create a frequency-dependent increase in resistance. Complex waveforms (other than sinusoidal) are composed of many frequencies and would be distorted by the coils. For instance, a step response of the coil pair (Fig. 7b inset) is followed by a 20 ms settling time of the generated magnetic field to the desired amplitude (Fig. 7b). For some predefined actuation waveforms, such as a square wave, open loop waveforms can be engineered to optimize settling [20], [21]. As an example, we show a unipolar overdrive (Fig. 7b inset) to improve the settling time more than 15-fold, achieving less than 2 ms (Fig. 7b).

Cumulatively, the presented platform is paves the way for many new experiments, including those utilizing feedback control. The real-time detection of contraction timing can be used to trigger a custom actuation waveform (such as square wave tension or mimicked contraction profile). The phase, or delay with respect to spontaneous contraction, can also be controlled and optimized. Moreover, most biological experiments have myriad variables and require multiple samples to generate statistics and prove an effect. The throughput and compactness of this platform enable simultaneous feedback of multiple tissues inside a standard incubator, ideal for such investigations.

V. DISCUSSION OF LIMITATIONS

The sensor and micromagnet are kept within the yellow region (Fig. 2c), where the uniform field from actuation varies by less than 5%, minimizing interference on the Hall sensor. It should be noted that this region is small (<125 mm^3), and instabilities in the magnetic field exist beyond the boundary. Coils without a cylindrical high-permeability shell will have fewer instabilities (Fig. S2), but more current is necessary to generate equivalent gradient field magnitudes. Asymmetry in coil construction (number of turns, etc.) and coil placement can vary in some setups. The voltage on each coil can be tuned independently to balance the magnetic field (Fig. 7a).

The detection resolution is primarily limited by the sensitivity of the Hall sensor to humidity and temperature (Fig. 3c), which was discovered during platform development. Although more expensive and less compact, magnetoresistive sensors have orders of magnitude better resolution and could be implemented in future designs, if desired. The interference of magnetic actuation with magnetic detection could be remedied by the addition of an inexpensive dummy sensor a minimum of a few millimeters away from the micromagnet, to subtract a calibrated interference in real time.

By applying a force to only one post in our design, we impose a force to both the microtissue, and, inadvertently, to the other post (Fig. S8). This creates an additional unknown during simultaneous actuation and detection that is difficult to control, and limits some, but not all feedback experimental designs. These two sources of pillar deflection can be isolated after post-processing of simultaneous microscope images and sensor voltages, but this is not ideal. Future designs may

extrude the width of the nonmagnetic post in the direction of tissue to effectively increase stiffness and cause deflection of only the magnetic post, as has been shown previously [17] and is discussed further (Fig. S8). Sustained large actuation (minutes to hours) also gives rise to coil heating. Although the coils are several centimeters away and may not affect the tissue, this may be mitigated. A smaller, custom petri dish could be developed to move the coils closer to the device, allowing for less current to be driven during actuation, decreasing heating.

VI. Conclusion

The results shown herein demonstrate a biocompatible platform that substantially opens the design space of the micromechanical environment of 3D biological tissues. A system with unique actuation and detection techniques was designed for enhanced mechanical control. Bidirectional actuation with an arbitrary waveform is achieved for greater than 200 μm displacements with high force resolution. Detection can be achieved simultaneously with the standard microscope and post-processing method, or with a Hall sensor, with options for real-time or recording and post-processing. Real-time detection of contractions is sufficient for mechanical feedback control contraction-triggered actuation experiments. For more complex feedback experiments, interference has been minimized for simultaneous magnetic actuation and detection, and suggestions have been made for further improvement.

Closed-loop experiments offer exciting, new experimental design. So far, open-loop experiments have already enabled the study of substrate stiffness [4], static stress [9], [10], mechanical training [13]–[16], and tissue strain characterization (such as the tissue length-dependent Frank-Starling relationship) [9]–[11]. Feedback enables unprecedented, dynamic control of biological tissue mechanics. In this paradigm, mechanical properties, such as damping and viscoelasticity, could be corrected for, or manipulated in real-time [27]–[29]. Such systems offer increased relevance to native biology, where self-sustaining homeostatic mechanisms are abundant. The presented platform has demonstrated the first step in this direction, enabling the feedback based on contraction-triggering in a scalable, compact platform.

Appendix

Supplementary information, including text, 8 figures, and 4 videos, is included in the *SI Appendix*.

Acknowledgment

References

[1] J. Javor, S. Sundaram, C. Chen, and D. J. Bishop, "Controlled strain of cardiac microtissue via magnetic actuation," in *Proc. IEEE 33rd Int. Conf. Micro Electro Mech. Syst. (MEMS)*, Jan. 2020, pp. 452–455.

[2] C. S. Chen, J. Tan, and J. Tien, "Mechanotransduction at cell-matrix and cell-cell contacts," *Annu. Rev. Biomed. Eng.*, vol. 6, no. 1, pp. 275–302, Aug. 2004.

[3] C. F. Guimaráes, L. Gasperini, A. P. Marques, and R. L. Reis, "The stiffness of living tissues and its implications for tissue engineering," *Nature Rev. Mater.*, vol. 5, no. 5, pp. 351–370, May 2020.

[4] E. Corbin, "Tunable and reversible substrate stiffness reveals dynamic mechanosensitivity of cardiomyocytes," *ACS Appl. Mater. Interfaces*, vol. 23, pp. 20603–20614, May 2019.

[5] M. Imboden et al., "High-speed mechano-active multielectrode array for investigating rapid stretch effects on cardiac tissue," *Nature Commun.*, vol. 10, no. 1, p. 834, Dec. 2019.

[6] T. Boudou et al., "A microfabricated platform to measure and manipulate the mechanics of engineered cardiac microtissues," *Tissue Eng. A*, vol. 18, nos. 9–10, pp. 910–919, May 2012.

[7] Y. Zhao, "A platform for generation of chamber-specific cardiac tissues and disease modeling," *Cell*, vol. 176, no. 4, pp. 913–927, 2019.

[8] K. Ronaldson-Bouchard, "Advanced maturation of human cardiac tissue grown from pluripotent stem cells," *Nature* vol. 556, no. 7700, p. 239, 2018.

[9] A. Leonard et al., "Afterload promotes maturation of human induced pluripotent stem cell derived cardiomyocytes in engineered heart tissues," *J. Mol. Cellular Cardiol.*, vol. 118, pp. 147–158, May 2018.

[10] J.-L. Ruan et al., "Mechanical stress conditioning and electrical stimulation promote contractility and force maturation of induced pluripotent stem cell-derived human cardiac tissue," *Circulation*, vol. 134, no. 20, pp. 1557–1567, Nov. 2016.

[11] N. Huebsch et al., "Miniaturized iPS-cell-derived cardiac muscles for physiologically relevant drug response analyses," *Sci. Rep.*, vol. 6, no. 1, Jul. 2016, Art. no. 24726.

[12] N. T. Feric and M. Radisic, "Towards adult-like human engineered cardiac tissue: Maturing human pluripotent stem cell-derived cardiomyocytes in human engineered cardiac tissues," *Adv. Drug Del. Rev.* vol. 96, p. 110, Oct. 2016.

[13] P. A. Galie, F. J. Byfield, C. S. Chen, J. Y. Kresh, and P. A. Janmey, "Mechanically stimulated contraction of engineered cardiac constructs using a microcantilever," *IEEE Trans. Biomed. Eng.*, vol. 62, no. 2, pp. 438–442, Feb. 2015.

[14] F. E. A. Xu, "A microfabricated magnetic actuation device for mechanical conditioning of arrays of 3D microtissues," *Lab Chip*, vol. 105, pp. 1293–1303, 2013.

[15] A. Marsano et al., "Beating heart on a chip: A novel microfluidic platform to generate functional 3D cardiac microtissues," *Lab Chip*, vol. 16, no. 3, pp. 599–610, 2016.

[16] A. Mihic et al., "The effect of cyclic stretch on maturation and 3D tissue formation of human embryonic stem cell-derived cardiomyocytes," *Biomaterials*, vol. 35, no. 9, pp. 2798–2808, Mar. 2014.

[17] D. Bielawski, "Real-time force and frequency analysis of engineered human heart tissue derived from induced pluripotent stem cells using magnetic sensing," *Tissue Eng.*, vol. 22, no. 10, pp. 932–940, 2016.

[18] E. De Lacheisserie, S. Tremolet, D. Gignoux, and M. Schlenker, *Magnetism*. vol. 1. Cham, Switzerland: Springer, 2005.

[19] (2020). *Allegro MicroSystems*. [Online]. Available: https://www.allegromicro.com/-/media/Files/Datasheets/A1359-Datasheet.ashx

[20] M. Imboden et al., "High-speed control of electromechanical transduction: Advanced drive techniques for optimized step-and-settle response of MEMS micromirrors," *IEEE Control Syst. Mag.*, vol. 36, no. 5, pp. 48–76, Dec. 2016.

[21] C. Pollock, "Extreme angle, tip-tilt MEMS micromirror enabling full hemispheric, quasi-static optical coverage," *Opt. express* vol. 27, no. 11, pp. 15318–15326, 2019.

[22] J. M. Cesaretti, W. P. Taylor, G. Monreal, and O. Brand, "Effect of stress due to plastic package moisture absorption in Hall sensors," *IEEE Trans. Magn.*, vol. 45, no. 10, pp. 4482–4485, Oct. 2009.

[23] M. D. Groner, F. Fabreguette, H. J. Elam, and W. George, "Low-temperature Al_2O_3 atomic layer deposition," *Chem. Mater*, vol. 4, no. 16, pp. 639–645, 2004.

[24] A. Stange, M. Imboden, J. Javor, L. K. Barrett, and D. J. Bishop, "Building a casimir metrology platform with a commercial MEMS sensor," *Microsyst. Nanoeng.*, vol. 5, no. 1, p. 14, Dec. 2019.

[25] J. Javor, A. Stange, C. Pollock, N. Fuhr, and D. J. Bishop, "100 pT/cm single-point MEMS magnetic gradiometer from a commercial accelerometer," *Microsyst. Nanoeng.*, vol. 6, no. 1, pp. 1–13, Dec. 2020.

[26] J. T. Hinson et al., "Titin mutations in iPS cells define sarcomere insufficiency as a cause of dilated cardiomyopathy," *Science*, vol. 349, no. 6251, pp. 982–986, Aug. 2015.

[27] M. Capitanio and F. S. Pavone, "Interrogating biology with force: Single molecule high-resolution measurements with optical tweezers," *Biophys. J.*, vol. 105, no. 6, pp. 1293–1303, Sep. 2013.

[28] Y. Li and C. Hierold, "SU-8 as a torsional spring: Viscoelastic creeping and closed loop control," *J. Microelectromech. Syst.*, vol. 24, no. 3, pp. 608–617, Jun. 2015.

[29] Y. K. Yong, A. J. Fleming, and S. O. Moheimani, "A novel piezoelectric strain sensor for simultaneous damping and tracking control of a high-speed nanopositioner," *IEEE/ASME Trans. Mechatronics*, vol. 18, no. 3, pp. 1113–1121, Jun. 2013.

Christopher S. Chen received the A.B. degree in biochemistry from Harvard, the M.S. degree in mechanical engineering from MIT, the Ph.D. degree in medical engineering and medical physics from the Harvard-MIT Health Sciences and Technology Program, and the M.D. degree from the Harvard Medical School. He is currently a Professor of biomedical engineering and the Director of the Tissue Microfabrication Laboratory, Boston University. He has been an instrumental figure in the development of engineered cellular microenvironments in order to engineer cell function. He serves as a Fellow of the American Institute for Medical and Biological Engineering, and as a member of the Faculty of 1000 Biology, the Board of Trustees for the Society for BioMEMS and Biomedical Nanotechnology, and Defense Sciences Study Group. He was previously an Assistant Professor in biomedical engineering and in oncology with Johns Hopkins University, the Skirkanich Professor of innovation, and a Founding Director of the Center for Engineering Cells and Regeneration, University of Pennsylvania.

Josh Javor received the B.S. degree in mechanical engineering from Ohio State University in 2016 and studied the electromagnetic detection of solid cancerous tumors for his Bachelor's thesis. He was then admitted into Boston University in the fall of 2016 to study MEMS/NEMS biomedical sensors for his Ph.D. thesis under the guidance of Dr. David J. Bishop. His research focuses on the development of tools to study the interaction of electromagnetic, mechanical, and electrical interactions with iPSC-derived cardiac tissue.

David J. Bishop (Member, IEEE) is currently the Director of CELL-MET, an NSF ERC, and also the Head of the Division of Materials Science and Engineering, Boston University. He is also a Professor of physics, Professor of mechanical engineering, Professor of electrical and computer engineering, a Professor of biomedical engineering, and a Professor of materials science and engineering at BU. Previously, he was the Interim Associate Dean for Research and Graduate Programs for the BU College of Engineering. Prior to joining BU, he was the Chief Technology Officer (CTO) and Chief Operating Officer (COO) of LGS. Before joining LGS, he was the President of Government Research and Security Solutions for Bell Labs, Lucent Technologies. In previous positions with Lucent, he served as a Nanotechnology Research VP for Bell Labs, Lucent Technologies; the President of the New Jersey Nanotechnology Consortium and the Physical Sciences Research VP.

Subramanian Sundaram (Member, IEEE) received the B.E. degree (Hons.) in electrical engineering and mechanical engineering from the Birla Institute of Technology and Science (BITS), Pilani, India, in 2010, and the S.M. and Ph.D. degrees in electrical engineering and computer science from the Massachusetts Institute of Technology (MIT), Cambridge, MA, in 2014 and 2018, respectively. He is currently an American Heart Association Postdoctoral Fellow with Boston University and the Wyss Institute for Biologically Inspired Engineering, Harvard University. His research interests include robotics, advanced fabrication, and tissue engineering.